Electrochimica Acta 176 (2015) 763–776

Contents lists available at ScienceDirect

Electrochimica Acta

journal homepage: www.elsevier.com/locate/electacta

Properties of the hydrogen oxidation reaction on Pt/C catalysts at optimised high mass transport conditions and its relevance to the anode reaction in PEFCs and cathode reactions in electrolysers

C.M. Zalitis[a,b], J. Sharman[b], E. Wright[b], A.R. Kucernak[a,*]

[a] Imperial College London, Department of Chemistry, London, SW7 2AZ, UK
[b] Johnson Matthey Technology Centre, Blounts Court Road, Sonning Common, Reading, RG4 9NH, UK

ARTICLE INFO

Article history:
Received 2 March 2015
Received in revised form 30 June 2015
Accepted 30 June 2015
Available online 14 July 2015

ABSTRACT

Using a high mass transport floating electrode technique with an ultra-low catalyst loading (0.84–3.5 $\mu g_{Pt}\,cm^{-2}$) of commonly used Pt/C catalyst (HiSPEC 9100, Johnson Matthey), features in the hydrogen oxidation reaction (HOR) and hydrogen evolution reaction (HER) were resolved and defined, which have rarely been previously observed. These features include fine structure in the hydrogen adsorption region between 0.18 < V vs. RHE < 0.36 V vs. RHE consisting of two peaks, an asymptotic decrease at potentials greater than 0.36 V vs. RHE, and a hysteresis above 0.1 V vs. RHE which corresponded to a decrease in the cathodic scan current by up to 50% of the anodic scan. These features are examined as a function of hydrogen and proton concentration, anion type and concentration, potential scan limit, and temperature. We provide an analytical solution to the Heyrovsky–Volmer equation and use it to analyse our results. Using this model we are able to extract catalytic properties (without mass transport corrections; a possible source of error) by simultaneously fitting the model to HOR curves in a variety of conditions including temperature, hydrogen partial pressure and anion/H^+ concentration. Using our model we are able to rationalise the pH and hydrogen concentration dependence of the hydrogen reaction. This model may be useful in application to fuel cell and electrolyser simulation studies.

1. Introduction

The hydrogen oxidation reaction (HOR), along with the hydrogen evolution reaction (HER) is one of the most studied reactions of modern science due to its simple reaction of one hydrogen molecule going to two protons, while releasing two electrons. This reaction also gains considerable attention as the anode reaction of a fuel cell. However, due to its facile nature, the kinetics have often been obscured by the relatively slow H_2 transport capabilities of the electrochemical cell. This is evident from room temperature (or room temperature corrected, where the activation energy was also stated) exchange current densities spanning three orders of magnitude in the literature, j_0 = ~0.2 – 60 mA cm^{-2} [1–11].

A previous paper by this group [12] showed ultra-high mass transport can be achieved on a floating electrode. This technique combined gaseous transport through a porous support and an ultra-thin catalyst layer to obtain a geometric peak current density of 5.7 A cm^{-2}_{Geo} for a 10.15 $\mu g_{Pt}\,cm^{-2}$ catalyst loading (60% Pt/C HiSPEC 9100 catalyst, Alfa Aesar). Assuming this peak current density was the absolute maximum geometric current density ($j_{Geo,max}$) for the technique, a corresponding mass transport coefficient (k_{MT}) equal to 58 cm s^{-1} was attained; equivalent to a rotation rate of ~4×10^9 rpm on the RDE. k_{MT} was calculated by combining the Faraday equation with Fick's law

$$k_{MT} = J/c_{H_2} \quad (1)$$

Where

$$J = j_{Geo,\max}/nF \quad (2)$$

J is the hydrogen flux, n = 2 for the HOR and c_{H2} is the concentration of hydrogen, taken as the saturation concentration in Nafion at 5.1×10^{-7} mol cm^{-3} [13]; due to the likelihood that a thin layer of liquid or Nafion covers the catalyst in this gas diffusion electrode [14,15]. This assumes the properties of the Nafion thin film layer remain the same as bulk Nafion.

It is worth noting that the real k_{MT} of the floating electrode technique is likely to be much greater as Fig. 10 in [12] shows that the geometric current density is still increasing linearly with

* Corresponding author. Tel.: +44 20 75945831.
E-mail address: anthony@imperial.ac.uk (A.R. Kucernak).

http://dx.doi.org/10.1016/j.electacta.2015.06.146

catalyst loading, with no sign of bulk mass transport effects, let alone a mass transport limitation.

k_{MT} is also likely to be very high for a fuel cell [11,16,17]. However, with a comparatively larger catalyst loading than the floating electrode, the rapid increase in current with over-potential for the HOR means the working limit of the potentiostat can be reached at small over-potentials. For example, to reach a current density of 600 mA cm^{-2}_{Spec} (as stated as the $j_{spec,max}$ in [12]), with an equivalent PEFC loading of 0.2 $mg_{Pt}\,cm^{-2}_{Geo}$ and a catalyst metal area of 89 $m^2\,g^{-1}$ (as the HiSPEC 9100 used in this study), the geometric current density would be over 100 A cm^{-2}_{Geo}. Even when reducing the catalyst loading, the area of a fuel cell electrode causes the absolute current density to be large. Neyerlin et al. [16] reached currents of 3 A cm^{-2}_{Geo} at only 60 mV vs. RHE with a 25 cm^2 electrode at a 35 $\mu g_{Pt}\,cm^{-2}$ catalyst loading, after correcting for iR losses. The effect of uncompensated resistance prevents the measurement of the HOR at higher over-potentials and could incur large errors from their correction.

The floating electrode technique uses small quantities of catalyst (sub 10 $\mu g_{Pt}\,cm^{-2}$) deposited uniformly and homogeneously across a small catalyst area (typically 1 mm radius spot, i.e. 0.0314 cm^2 geometric area) which gives three advantages: such a thin catalyst layer allows all the catalyst to see an equivalent environment, giving access to electrochemical fine structure (e.g. peaks) which would otherwise be blurred in an electrode with a gradient of conditions across or through its catalyst layer; the absolute current remains low (mA's equivalent to A cm^{-2} geometric current), even at high over-potentials, reducing the possible errors from correcting for *iR* effects and local Joule heating effects; and small amounts of catalyst are needed for one test, making it beneficial to test novel catalysts produced in small quantities. This allows the floating electrode to be an advantageous technique for testing novel fuel cell catalysts ex-situ while retaining the high mass transport conditions expected in a PEFC.

Additionally, a benefit over the RDE technique is that as the electrolyte is stationary, convective transport of environmental contaminants (chloride etc.) is significantly reduced, leading to better performance in the presence of even vanishingly small quantities of solution impurities.

From these benefits, the floating electrode gives an idealised environment to measure the HOR/HER, defining features which have rarely been observed. These features include fine structure in the hydrogen adsorption region between 0.18 and 0.36 V vs. RHE consisting of two peaks, an asymptotic decrease at potentials greater than 0.36 V vs. RHE, and a hysteresis above 0.1 V vs. RHE. This paper explains these features in terms of surface adsorbed species and edge and facet sites on the catalyst. In addition, intrinsic catalyst properties are extracted using a numerical model to fit the HOR curves in a variety of conditions including temperature, hydrogen partial pressure and anion/H^+ concentration.

2. Experimental

A commercial 60 wt.% Pt/C catalyst (HiSPEC 9100, Alfa Aesar, metal area of 89 $m^2\,g^{-1}$ [18]) and high purity gases (N_2, H_2 and O_2 at >5.8 N from Air Products) and acids were used; perchloric acid from VWR (Merc Suprapur) and GFS chemicals (Veritas double distilled) were both used with negligible difference in performance (not shown) and sulfuric acid from VWR (Aristar grade). The electrodes were made up as in [12]. Polycarbonate track etched membranes (Sterlitech, PCTF0447100, 0.4 μm pores) were coated with 100 nm of gold by sputter deposition, and after deposition of the catalyst, the pores were hydrophobised with an amorphous fluoropolymer (Teflon AF 2400, 2.1 $\mu g\,cm^{-2}_{Geo}$). The catalyst was deposited via the vacuum filtered catalyst (VFC) method described in [12] to achieve uniform and homogeneous catalyst spots at ultra-low catalyst loadings ($\mu g_{Pt}\,cm^{-2}$) from a dilute catalyst ink. The ink makeup was optimised to use small quantities of catalyst (typically 1 mg), especially useful for novel catalysts synthesised in small quantities. A stock ink containing a catalyst to solvent ratio of 1:10 (mg:ml); the solvent contained 50% butyl acetate (Sigma, anhydrous grade) and 50% from a mix of propan-2-ol (VWR, Normapur analytical reagent) and the PFSA solution (DuPont DE521 Nafion solution, 5 wt%) to give a catalyst to PFSA ratio of 1:1 (volume). An aliquot of this stock catalyst ink was then diluted to 500 μl with a 50:50 mix of butyl acetate and propan-2-ol to

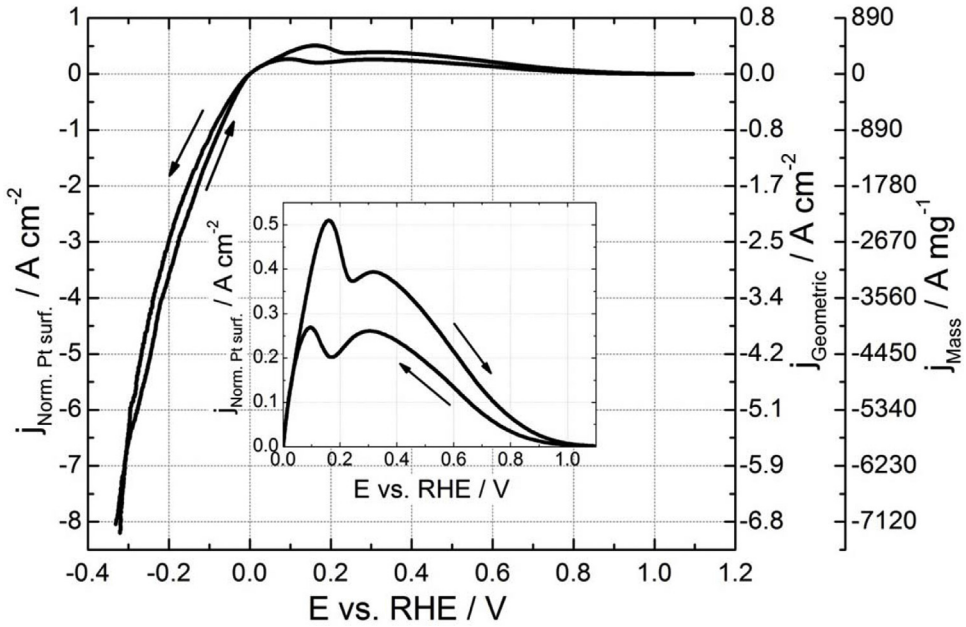

Fig. 1. Voltammogram of the HOR and HER on HiSpec 9100 60% Pt/C catalyst at a loading of 0.84 $\mu g_{Pt}\,cm^{-2}$. 101 kPa H_2, 4 mol dm^{-3} $HClO_4$, 298 K, 10 mV s^{-1}. The ordinate axis corresponds to the specific current density (left), geometric current density (first right) and mass activity (second right), refer to Eq. (25) for relation between the units.

produce the required loading (see reference [12] to correct for loss of catalyst through the pores).

The performances of the floating electrodes were measured with a Gamry Reference 600 potentiostat in a water jacketed three electrode electrochemical cell utilizing a Pt counter electrode and a RHE in a Luggin capillary configuration. These electrodes were floated on liquid electrolytes with the reactant gas supplied to the catalyst through the hydrophobised pores, allowing high mass transport. 4 mol dm^{-3} perchloric acid was used to minimise the uncompensated resistance at the high currents achieve from the HOR, unless otherwise stated. Conditioning the electrodes by switching between a HOR scan (100% H_2, 50 mV s^{-1}, −0.1–1 V vs. RHE) and an ORR scan (100% O_2, 50 mV s^{-1}, 1.1–0.3 V vs. RHE), with an intermediate N_2 purge, 10 times or until the scan was repeatable at 25 °C was found to improve the repeatability of the measurement across electrodes, while no loss of performance was observed due to degradation. The cell was held at the relevant temperature using a re-circulator (Polyscience digital temperature controller, ±0.1 °C). Gas mixtures were obtained using gas flow controllers (Bronkhurst EL flow series). Uncompensated resistances were corrected using the high frequency intercept of impedance measurements at a range of voltages.

To measure the potential of zero total charge (PZTC), CO displacement was recorded by dosing the electrode with CO at a range of potentials while recording the current, a method described in detail in [19,20]. This technique assumes CO is a strong adsorbate, able to displace all of the previously adsorbed species, however, the technique cannot distinguish between species of the same charge. As CO is a neutral species, CO displacement causes a quantity of charge associated with the desorption (e^-) of the previous species to be released, as shown in Eqs. (3) and (4) for hydrogen and anion (A) species with partial charge transfer (δ), respectfully.

$$Pt - H + CO \rightarrow Pt - CO + H^+ + e^- \tag{3}$$

$$Pt - A^{(1-\delta)-} + CO + \delta e^- \rightarrow Pt - CO + A^- \tag{4}$$

3. Results and discussion

Fig. 1 shows a typical CV of the HOR (Expanded in the inset) using the ultra-low catalyst loading floating electrode technique (loading = 0.84 $\mu g_{Pt}\,cm^{-2}$). The scan also extends into the HER region. The HOR shows fine structure in the hydrogen adsorption region between 0.18 and 0.36 V vs. RHE consisting of two peaks (herein called $E_{Peak,low}$ and $E_{Peak,high}$ for the peak at the lower and higher potential, respectively), an asymptotic decrease at potentials greater than 0.36 V vs. RHE, and a hysteresis above 0.1 V vs. RHE which corresponds to a decrease in the cathodic scan current by up to a half in comparison to the anodic scan; as reported previously [12,15]. For the HER, the current density reached 8 A cm^{-2}_{Spec} at a potential of -0.33 V vs. RHE with no sign of a limitation, or current disruption from bubble formation. Such high current densities without bubble formation, and hence potential disruption of the catalyst layer, are unparalleled and are typically the limiting factor for measuring the HER on the RDE. Instead, the voltammogram remained smooth; confirming the fast mass transport of H_2 gas from the catalyst that this floating electrode technique is capable of. The current density at the cathodic scan limit corresponds to a H_2 turnover number on Pt of >19000H_2 molecules per surface platinum atom per second, or equivalently a mass activity of over 7 MA g_{Pt}^{-1}!

The $E_{peak,low}$ of the HOR at 0.18 V vs. RHE has a current density of 0.51 A cm^{-2}_{Spec}, corresponding to a turnover number of 1200H_2 molecules per surface platinum atom per second. Previously, we showed that the peak current density remains constant at 0.6 ± 0.06 A cm^{-2}_{Spec} with no decrease in current density as the catalyst loading increased from 0.72 to 10.15 $\mu g_{Pt}\,cm^{-2}$, showing no bulk mass transport limitations [12]. The HER current density at the cathodic limit is greater than ten times the current density of the HOR limiting current density, and as the transportation of H_2 away from the electrode looks adequate (i.e. no bubble formation); it is logical to assume this electrode is capable of supplying H_2 to the electrode at the same rate. This adds further confirmation that the peak current density is related to an electrokinetic or adsorption step at the Pt surface such as a hydrogen adsorption limitation or a local hydrogen or proton transport limitation; possibly caused by a thin layer of Nafion or water as discussed in [15].

3.1. HOR reaction

As our purpose in this paper is to consider some aspects of the hydrogen oxidation reaction close to the equilibrium potential, we will used a simplified model which neglects both the potential dependence of adsorption site density, and assumes Heyrovsky–Volmer kinetics.

$$H_2^{bulk} \xrightarrow{k_{MT,gas}} H_2^{surf} \tag{5}$$

$$Pt + H_2^{surf} \underset{k_{-1}}{\overset{k_1}{\leftrightarrows}} H_3O^{+,surf} + Pt - H_{ad} + e^- \tag{6}$$

$$Pt - H_{ad} + H_2O^{surf} \underset{k_{-2}}{\overset{k_2}{\leftrightarrows}} H_3O^{+,surf} + Pt + e^- \tag{7}$$

$$H_3O^{+,surf} \underset{k_{MT,liq}}{\overset{k_{MT,liq}}{\leftrightarrows}} H_3O^{+,bulk} \tag{8}$$

Where $k_{MT,gas}$ and $k_{MT,liq}$ are the mass transport coefficients in gas and liquid respectively. We will assume for simplicity that that mass transport of reactant and products are fast (although see above), and so we only consider Eqs. (6) and (7). Although we do not explicitly include water within the kinetic equations as it acts as a solvent in our system, it might be important to include this parameter under fuel cell systems, especially when operating at low relative humidities. Eqs. (6) and (7) can be analytically solved under steady state conditions, and we will provide a full derivation in a future paper, however an abbreviated derivation follows. The hydrogen coverage, under steady-state conditions can be found by finding the solution to the equation

$$\begin{aligned}\frac{d\theta_{H_{ad}}}{dt} &= k_1 a_{H_2^{surf}}(1-\theta_{H_{ad}}) - k_{-1} a_{H_3O^{+,surf}} \theta_{H_{ad}} - k_2 \theta_{H_{ad}} \\ &\quad + k_{-2} a_{H_3O^{+,surf}}(1-\theta_{H_{ad}}) \\ &= 0\end{aligned} \tag{9}$$

where $\theta_{H_{ad}}$ is the surface coverage of adsorbed hydrogen. Solution of (9) provides

$$\theta_{H_{ad}} = \frac{k_1 a_{H_2^{surf}} + k_{-2} a_{H_3O^{+,surf}}}{k_1 a_{H_2^{surf}} + k_2 + k_{-1} a_{H_3O^{+,surf}} + k_{-2} a_{H_3O^{+,surf}}} \tag{10}$$

This provides us the hydrogen coverage which then combined with the equations for electrochemical current generation

$$j/F = k_1 a_{H_2^{surf}}(1-\theta_{H_{ad}}) - k_{-1} a_{H_3O^{+,surf}} \theta_{H_{ad}} + k_2 \theta_{H_{ad}} - k_{-2} a_{H_3O^{+,surf}}(1-\theta_{H_{ad}}) \quad (11)$$

allows calculation of the electrochemical current under any conditions. Under equilibrium conditions (i.e. at the reversible potential as defined by $a_{H_3O^{+surf}}$ and $a_{H_2^{surf}}$ and denoted by superscript "*eq*"), $\theta_{H_{ad}}$ in Eq. (10) becomes $\theta^{eq}_{H_{ad}}$, j in Eq. (11) becomes zero and all the k's in both equations become k^{eq}'s. Simultaneous solution of both of these equations under equilibrium conditions leads to the equality

$$\frac{k_2^{eq}}{k_{-2}^{eq} a_{H_3O^{+,surf}}} = \frac{k_{-1}^{eq}}{k_1^{eq}} \frac{a_{H_3O^{+surf}}}{a_{H_2^{surf}}} \quad (12)$$

Hence we define a constant K, such that

$$K = \frac{k_2^{eq}}{k_{-2}^{eq} a_{H_3O^{+,surf}}} \therefore k_{-2}^{eq} = \frac{k_2^{eq}}{K a_{H_3O^{+,surf}}}, k_{-1}^{eq} = K k_1^{eq} \frac{a_{H_2^{surf}}}{a_{H_3O^{+,surf}}} \quad (13)$$

Substitution of k^{eq}_{-2} and k^{eq}_{-1} into in Eq. (10) under equilibrium conditions provides the hydrogen coverage at the equilibrium potential

$$\theta^{eq}_{H_{ad}} = \frac{1}{1+K} \quad (14)$$

In order to introduce the electrochemical potential into the kinetic equations, we assume that as the applied potential is altered from the equilibrium potential by $\eta = E\text{-}E_{eq}$, the k's take the form

$$k_1 = k_1^{eq} e^{\alpha f \eta},$$

$$k_{-1} = k_{-1}^{eq} e^{-(1-\alpha) f \eta} = K k_1^{eq} \frac{a_{H_2^{surf}}}{a_{H_3O^{+,surf}}} e^{-(1-\alpha) f \eta},$$

$$k_2 = k_2^{eq} e^{\alpha f \eta},$$

$$k_{-2} = k_{-2}^{eq} e^{-(1-\alpha) f \eta} = \frac{k_2^{eq}}{K a_{H_3O^{+,surf}}} e^{-(1-\alpha) f \eta}$$

$$f = \frac{F}{RT} \quad (15)$$

Where $f = F/RT$, with their usual meanings. Substituting into Eqs. (10) and (11) provides the potential dependence of hydrogen coverage and current density

$$\theta_{H_{ad}}(\eta) = \frac{k_1^{eq} a_{H_2^{surf}} e^{\alpha f n} + \frac{k_2^{eq}}{K} e^{-(1-\alpha) f \eta}}{(k_1^{eq} a_{H_2^{surf}} + k_2^{eq}) e^{\alpha f \eta} + (K k_1^{eq} a_{H_2^{surf}} + \frac{k_2^{eq}}{K}) e^{-(1-\alpha) f \eta}} \quad (16)$$

$$j = F\Big(\Big(k_1^{eq} a_{H_2^{surf}}(1-\theta_{H_{ad}}(\eta)) + k_2^{eq}\theta_{H_{ad}}(\eta)\Big) e^{\alpha f \eta} - \Big(K k_1^{eq} a_{H_2^{surf}} \theta_{H_{ad}}(\eta) + \frac{k_2^{eq}}{K}(1-\theta_{H_{ad}}(\eta))\Big) e^{-(1-\alpha) f \eta}\Big) \quad (17)$$

It can be seen that j depends in a complicated way on$K, k_1^{eq}, k_2^{eq}, a_{H_2^{surf}}$ and (through K), $a_{H_3O^{+,surf}}$. For instance, when the Heyrovsky step is fast compared to the Volmer step, then a first order dependence in hydrogen concentration is expected. If we assume that both Heyrovsky and Volmer step show the same activation energy then we can include the temperature dependence through the Arrhenius equation (assuming a standard temperature of 298 K for T*)

$$j = F\Big(\Big(k_1^{eq} a_{H_2^{surf}}(1-\theta_{H_{ad}}(\eta)) + k_2^{eq}\theta_{H_{ad}}(\eta)\Big) e^{\alpha f n} - \Big(K k_1^{eq} a_{H_2^{surf}} \theta_{H_{ad}}(\eta) + \frac{k_2^{eq}}{K}(1-\theta_{H_{ad}}(\eta))\Big) e^{-(1-\alpha) f n}\Big) e^{\frac{-E_a}{R}\left(\frac{1}{T}-\frac{1}{T^*}\right)} \quad (18)$$

where E_a is the activation energy of the reaction. Provided $\eta \ll \alpha f$, we can take the series expansion of this equation (having expanded $\theta_{H_{ad}}(\eta)$ in terms of Eq. (16)) about $\eta = 0$ to provide an estimate of the current close to the equilibrium potential

$$j(\eta) \cong \frac{F}{RT}\left(\frac{4F\theta^{eq}_{H_{ad}}}{\frac{1}{K k_1^{eq} a_{H_2^{surf}}} + \frac{1}{k_2^{eq}}}\right) \eta e^{\frac{-E_a}{R}\left(\frac{1}{T}-\frac{1}{T^*}\right)} \quad \eta \ll \alpha f$$

$$j(\eta) \cong \frac{F}{RT} j_o \eta e^{\frac{-E_a}{R}\left(\frac{1}{T}-\frac{1}{T^*}\right)} \quad (19)$$

Hence we see that close to the equilibrium potential, the exchange current density is a composite associated with the Heyrovsky and Volmer reactions in series. Limiting values for hydrogen concentration dependence are first order ($K k_1^{eq} a_{H_2} \gg k_2^{eq}$) or zeroeth order for the opposite case. Depending on the magnitude of K, limiting values of first order dependence ($K >> 1$) or zeroth-order dependence ($K << 1$) may be seen for hydrogen ion concentration. Of course, it is also possible to have intermediate concentration dependence or a transition depending on the ranges over which the reactants are changing.

Eq. (19) can be used to fit the linear region of a current voltage curve for the *hor*/*her* utilising the three kinetic parameters as fitting parameters $(K, k_1^{eq}, k_2^{eq}, E_a)$, or a simpler form of the equation may be used to estimate which domain we are operating in. In this case, Eq. (19), may be simplified to the form

$$j(\eta) \cong \frac{4F^2}{RT} k_{0,obs} \left(a_{H_2^{surf}}\right)^{\gamma} \left(a_{H_3O^{+,surf}}\right)^{\varepsilon} \eta e^{\frac{-E_a}{R}\left(\frac{1}{T}-\frac{1}{T^*}\right)} \eta \ll \alpha f \quad (20)$$

Where $k_{0,obs}$ is an effective rate constant assuming the values of K, k_1^{eq}, k_2^{eq} are such that the reactant concentration dependence are separable from Eq. (19) (i.e $K k_1^{eq} a_{H_2^{surf}} \gg k_2^{eq}$ or $K k_1^{eq} a_{H_2^{surf}}$ and $K >> 1$ or $K << 1$). A formula similar to Eq. (20) is often used in previous literature without appreciation of the conditions under which it is applicable. Under these simplifying conditions

$$j(\eta) \cong \frac{F}{RT} j_{0,obs} \eta e^{\frac{-E_a}{R}\left(\frac{1}{T}-\frac{1}{T^*}\right)} \quad \eta \ll \alpha f$$

$$j0,obs = 4F k_{0,obs} \left(a_{H_2^{surf}}\right)^{\gamma} \left(a_{H_3O^{+,surf}}\right)^{\varepsilon} \quad (21)$$

It is important to note that if the above criteria are not met, then this simplified form is not applicable, and inconsistent results will be obtained. One example of such inconsistent results will be non-linearity in the reactant stoichiometry plots (Log(j_o) vs log ($a_{reactant}$)), although in practice many ignore such nonlinearities and attempt to force a linear fit.

In the above analysis, we have for simplicity assumed that the number of available sites for adsorption is $(1-\theta_{H_{ad}})$. In fact, as we will show below, the situation is somewhat more complicated and that the number of available sites for adsorption, especially at higher potentials may be much less than this term suggests. A more accurate approach may be to write this term as $(1-\theta_{Spectator}-\theta_{H_{ad}})$ where the extra term is associated with the species that adsorb more strongly than the hydrogen on the surface. The change in a_{H_2} is the activity of dissolved hydrogen and

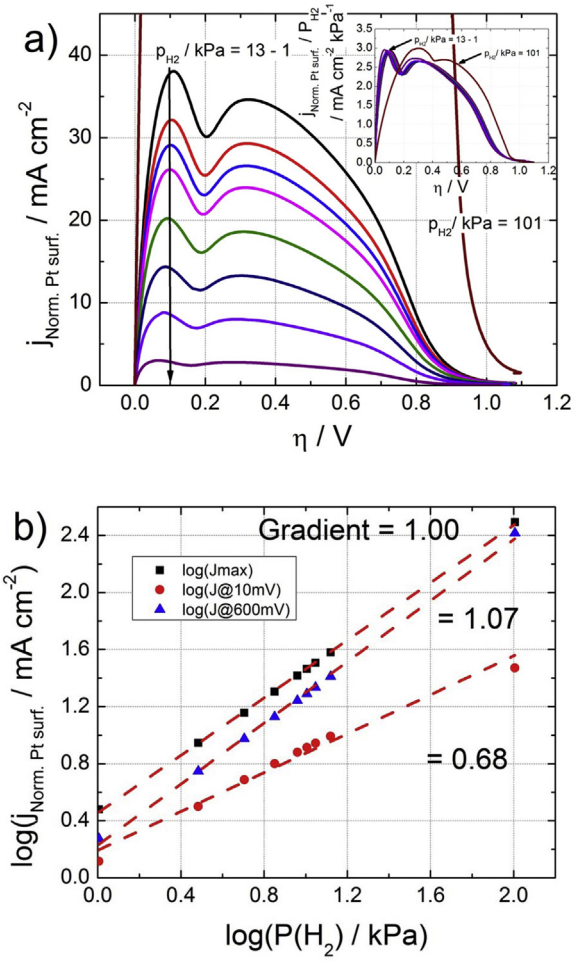

Fig. 2. a) Hydrogen partial pressure dependence of a 3.5 $\mu g_{Pt}\,cm^{-2}$ HiSpec 9100 60% Pt/C electrode in 0.5 mol dm^{-3} $HClO_4$. H_2 partial pressure (N_2 diluent, uncorrected for water vapour): 1.00, 0.13, 0.11, 0.09, 0.07, 0.05, 0.03, 0.01;, 298 K, 10 mV s^{-1}. RE = RHE. The x-axis has been converted to over-potential, accounting for the change in equilibrium potential with hydrogen partial pressure through the Nernst equation. Inset shows the curves normalised to the partial pressure of hydrogen. b) shows the log(j_{Spec}) vs. log(p(H_2)) of the curves.

equivalent to the change in partial pressure of hydrogen, P_{H_2}, assuming Henry's Law

$$a_{H_2} = a_{H_2^*}\left(\frac{P_{H_2}}{P_{H_2^*}}\right) \approx c_{H_2^*}\left(\frac{P_{H_2}}{P_{H_2^*}}\right) \tag{22}$$

Where $a_{H_2^*}$ and $P_{H_2^*}$ are the saturation activity and partial pressure of pure hydrogen at standard conditions.

3.2. Hydrogen concentration dependence

Fig. 2a) shows the anodic scans of the HOR in pure H_2 and at different H_2 partial pressures between $1 \le p(H_2) \le 101$ kPa in N_2. The x-axis is plotted in terms of over-potential (η), denoting that the potential scale has been corrected for the shift in equilibrium potential (E_e) for the set conditions through the Nernst equation, in the rearranged form of Eq. (23).

$$E_e = E^0 - \frac{2.303RT}{nF}\log\left(\frac{\sqrt{a_{H_2}} \times a_{H_2O}}{a_{H_3O^+}}\right) \tag{23}$$

Where E^0 is the standard potential and a_x denotes the activity of species x. The change in a_{H_2} is equivalent to the change in partial pressure of hydrogen, P_{H_2}, assuming Henry's Law, Equation. Although in the experiments presented here, $a_{H_2O} = 1$, as water is the solvent, we explicitly include the water term as within a fuel cell water activity may vary with operating conditions.

As the partial pressure increased, the current density increased in a near linear fashion. Inset into Fig. 2a) are the plots of the current densities ratioed to hydrogen partial pressure in each plot, it can be seen that surprisingly there is little variation. $j_{Peak,high}$ retains its relative height, and the decay in current at higher potentials follows the same form. There is a slight shift in the potential of $E_{Peak,low}$ towards lower potentials with decreasing hydrogen partial pressure; this is especially visible when comparing to the HOR in pure H_2, where it has shifted by ~0.2 V. While these curves are *iR* corrected, this shift could be due to an additional uncompensated resistance, but attempts to correct the data show that the added effect is not a linear function of current. A second hypothesis might be that the proton activity is being varied at the catalyst surface due to a proton gradient at the interface (i.e. diffusion of protons to/from the catalyst surface), and this is producing a Nernstian shift in the equilibrium potential. A final possibility is that the potential shift is a manifestation of a mass transport effect – that is we are seeing a concentration overpotential effect. A full discussion of these effects will be presented in a separate paper [21].

We determine the experimental reaction order (γ) of hydrogen from the gradient of log(j) vs log(P_{H2}), assuming Henrys law holds and that mass transport effects are not too great. Fig. 2b) shows this plot, linear gradients are obtained across the entire potential region, and three examples are plotted; j_{Max}, j_{10mV} and J_{600mV}.The gradients of j_{Max} and j_{600mV} gave values close to $\gamma = 1$. This is in agreement with what Wang et al.'s [11] observed for a PtCoMn alloy. While the gradient of j_{10mV} falls below this at $\gamma = 0.7$. These results may be rationalised in terms of Eq. (18). If we assume that at positive overpotentials, hydrogen coverage decreases (as is commonly considered), we see that as the overpotential increases, we more favour the k_1^{eq} terms (forward and reverse Heyrovsky reactions) which both show a first order dependence on hydrogen concentration. This means that at large positive overpotentials we are liable to see a first order dependence with hydrogen concentration. As the overpotential approaches the equilibrium potential, the situation may become less clear cut, and the zeroeth order dependence of the Volmer reaction (k_2^{eq}) will have a tendency to decrease the observed hydrogen concentration dependence, which may drop below 1, as seen in our results. This is confirmed by the constant $j_{Spec,max}/P_{H2}$ values for the different pressures at ~3 mA cm^{-2} kPa^{-1} shown in the inset of Fig. 2(a).

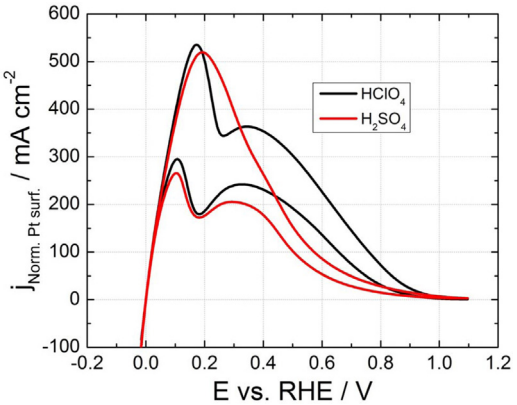

Fig. 3. Anion effect for different acids on a 1.7 $\mu g_{Pt}\,cm^{-2}$ HiSpec 9100 60% Pt/C electrode in 4 mol dm^{-3} $HClO_4$ and 4 mol dm^{-3} H_2SO_4. 101 kPa H_2, 298 K, 10 mV s^{-1}.

3.3. Anion Species

To test the effect of anion adsorption on the HOR, two electrolytes commonly used for their so called specifically and non-specifically adsorbed anions were used; sulfuric and perchloric acid. Anion interaction at the electrode surface has been shown to have a strong displacement and blocking effect on the ORR; the stronger the adsorption, the greater the blocking effect [22]. As the electrocatalyst is bound with Nafion ionomer, we may also expect some effect due to the teathered sulfonate groups which have been previously shown to lead to strong anion adsorption effects [13,23].

Fig. 3 shows the HOR using the floating electrode in both electrolytes. Close to the origin and going up to $E_{Peak,low}$, the activity of the electrode in the two acids appears very similar. The potential of $E_{Peak,low}$ in the two electrolytes are within 20 mV of each other. Therefore, in the region below $E_{Peak,low}$, no effect of anion adsorption was observed and we conclude the exchange current density can be measured in either acid with no significant difference. This is in agreement with Rau et al. [24] when using polycrystalline Pt with no perflorosulfonic ionomer (PFSI). The lack of interference is most probably due to the potential being below the PZTC, where anion adsorption is minimal, as discussed below. This is also shown in Table 1 and Fig. 5 below, where the exchange current density is the same in sulfuric acid as it is in perchloric acid for equivalent acid concentrations.

As the potential passes $E_{Peak,low}$, however, there begins to be a significant difference between the two electrolytes. While the HOR activity decays in both solutions, in ionomer/perchloric acid, a 5 fold decrease in activity is seen between 0.2 and 0.8 V vs. RHE (before oxide formation is thought to begin), but in sulfuric acid, the stronger adsorbing anion, the magnitude of $E_{peak,high}$ is significantly suppressed, and the HOR remains suppressed well into high potentials (>0.8 V vs. RHE); leading to a 10 fold decrease in activity between 0.2 and 0.8 V vs. RHE. The extra suppression over perchloric acid can also be seen clearly on the reverse scan. This suggests both electrolyte systems cause perturbation to the HOR, with the stronger anion giving a stronger perturbation. Kita et al. [25] performed experiments on single crystal platinum electrodes in static electrolytes and observed a decrease in activity at higher potentials (ca, 0.5 V vs. RHE), with a more pronounced decrease or stronger inhibition for sulphuric acid then perchloric acid, similar to in Fig. 3. They proposed that as perchloric acid is not a specifically adsorbing anion, the HOR inhibition in perchloric acid must be down to reorientation of surface water molecules in the double layer. In contrast we consider that perchlorate does adsorb to a small extent, especially as the perchlorate ion is at a high concentration (4 mol dm^{-3}) in this experiment. This conclusion is also supported by recent work by Omura et al. [26] who through quartz crystal microbalance and IR spectroscopy see indications of perchlorate adsorption at higher potentials. The potential dependence of this inhibition is explored further in the sections Platinum PZTC and Hysteresis of the HOR. In these electrodes, which utilise a small quantity of PFSI binder, it might be expected that some effect of anion adsorption from the relatively strongly adsorbing sulfonic acid groups of the PFSI might have some contribution to the shutdown of hydrogen oxidation at higher potential. However, due to the low coverage of the sterically hindered sulfonate groups limited surface coverage (estimated at ~0.1 monolayers on Pt(111)) [23], it is unlikely to be the major cause the 5 fold decrease in activity observed between 0.2 and 0.8 V vs. RHE here.

Bagotzky and Osetrova [1] observed HOR inhibition from Br and I anion adsorption which shows the greater the anion adsorption strength, the greater the kinetic inhibition. Although we cannot exclude the possibility of some very small amount of free chloride in our electrolyte (a contaminant in even the most stringently prepared perchloric acid), we have performed dosing experiments which suggest that the level is less than 0.4 μmol dm^{-3}. Furthermore, a tremendous benefit of our approach compared to RDE experiments is the absence of forced convection. Hence the transport of adventitious poisons is much slower (ca. 100-fold) compared to RDE measurements where the diffusion layer is much thinner (ca. 1 μm) compared to the boundary layer in quiescent electrolyte (ca. 100 μm).

Hence there is a clear indication that the HOR is affected by anion adsorption above the $E_{Peak,low}$. The reduced activity for the HOR covers the entire potential region of the ORR, and agrees with the reduced activity of the ORR seen in sulfuric acid in comparison to perchloric acid. In this sense, Wiberg et al. [27] correlated the inhibition of the HOR with oxide coverage (generally >0.8 V vs. RHE) on a polycrystalline Pt disk RDE and applied this surface blocking coverage to the ORR. The floating electrode technique should allow the HOR to be used as a probe for the state of the Pt surface across the entire ORR potential window.

3.4. Proton Activity

Fig. 4 and Table 1 show the effect of electrolyte pH and ionic strength on the activity of the HOR in a) perchloric acid and b) sulfuric acid between 0.1–4 mol dm^{-3}. A decrease in the gradient

Table 1
Properties of the HOR at 298 K, 101 kPa H_2 in different electrolytes. Exchange current densities calculated using Eq. (21).

Electrolyte conc./mol dm^{-3}		pH	j_0*/mA cm^{-2}	$E_{Peak,low}$/V vs. RHE	R_{HFR} †/Ω	Predicted R_{soln}‡/Ω
$HClO_4$						
4		−0.6	128	0.18	1.2	1.4
1.59		−0.2	92	0.24	2.4	2.1
0.63		0.2	82	0.30	5.1	4.2
0.25		0.6	50	0.40	11	10
0.1		1	32	0.54	25	26
$HClO_4$	$NaClO_4$					
4	0	−0.6	150	0.16	3.1	2.8
0.4	3.6	0.4	38	0.31	3.6	5.9
H_2SO_4						
4		−0.6	138	0.20	1	1.3
2		−0.3	118	0.20	1.5	1.7
0.5		0.3	70	0.27	4.8	4.8
0.1		14	28	0.51	17	23

*Calculation of "simple" exchange currents is discussed in Section 3.5, using Eq. (21). No correction made for water vapour.
†High frequency resistance measured using electrochemical impedance spectroscopy.
‡Resistance (R) calculated using conductivity values from [28] for $HClO_4$ and H_2SO_4 and [42] for $NaClO_4$, the distance between the WE and RE (l) is 0.5 cm apart from the mixed electrolyte section ($HClO_4$ + $NaClO_4$) in which the gap was 1 cm. For the mixed electrolyte, it is a combined resistance assuming negligible effect of ionic activity coefficients.

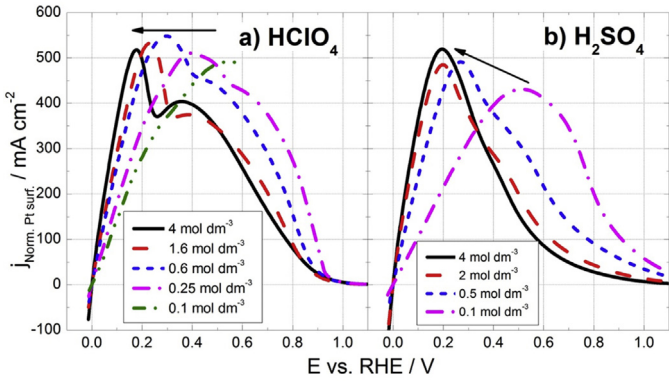

Fig. 4. Electrolyte concentration effect: Voltammograms of the HOR with a 1.4 $\mu g_{Pt}\,cm^{-2}$ Pt/C catalyst run in a range of electrolyte concentrations of both perchloric and sulphuric acid. 101 kPa H_2, 10 mV s^{-1}, 298 K. Voltammograms are iR corrected using electrochemical impedance data.

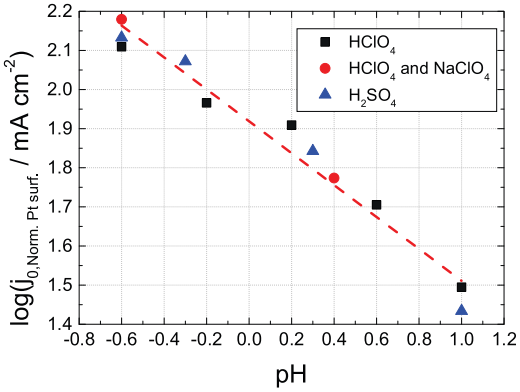

Fig. 5. The dependence of pH on the logarithm of the exchange current density of the different electrodes presented in Table 1, giving a gradient of about −0.4. Temperature: 298 K, 101 kPa H_2.

across the polarisation region and peak shift to higher potentials is clearly observed in both solutions. As there was no supporting electrolyte in these experiments, the resistance also increased with reducing acid concentration, and was corrected using the high frequency intercept from impedance spectra. To check that the *iR* correction wasn't introducing a systematic error, experimental spectra were collected for an electrode placed in 4 mol dm^{-3} perchloric acid and 0.4 mol dm^{-3} perchloric acid plus 3.6 mol dm^{-3} sodium perchlorate electrolytes. For these two electrolytes the perchlorate anion concentration was the same, and the resistance did not change too significantly (results shown in Table 1). For the 0.4 mol dm^{-3} perchloric acid with 3.6 mol dm^{-3} sodium perchlorate support, both the exchange current density and peak potential correlated well to results in 0.4 mol dm^{-3} perchloric acid without sodium perchlorate. In addition, the theoretical resistance was calculated assuming a distance between the working and reference electrode of 0.5 cm and the molar conductivity of the respective electrolytes from [28], which also correlated well with the experimentally measured resistances.

We postulate that two effects dominate the CVs as the proton concentration decreases:

1) A change in local proton concentration

As calculated above, 1200H_2 molecules are oxidised per surface platinum atom per second at the peak current density. This rapid production in protons local to the catalyst surface is likely to have an effect on the local proton activity. A local pH change would shift the Nernstian reversible potential and appear as an apparent increase in polarisation, shifting the peak to higher potentials (appearing like a resistance), and is likely to be the cause of the peak broadening. In effect this is a mass transport effect, but of the product, not the reactant. While this change in local pH should be prevented by the principle of charge neutrality and possibly even more so in our system where the presence of PFSI in the catalyst layer should create a fixed layer of sulfonate anions at the surface which would likely prevent large pH, we believe it cannot be discounted. Bagotzky and Osetrova [1] observed this effect when using a very thin film of electrolyte across a microelectrode. They concluded that transport of protons away from the catalyst surface was limited by the thin film and removed the effect by increasing the film thickness. However, a thicker film caused a larger barrier for H_2 diffusion through which would decrease measured peak current densities. The opposite effect has been recognised at microelectrodes during the HER, leading to proton depletion near the electrode, and hence an increase in local solution resistance, and enhanced proton migration [29,30]. In this study, most results used a high acidity electrolyte (4 mol dm^{-4} or pH −0.6) to reduce any change in local pH.

2) An effect of proton concentration on the exchange current density

At low current densities, the production of protons is not so rapid, therefore the decreased gradient is not likely to be related to a local pH change alone. Fig. 5 shows the pH dependence of the logarithm of exchange current density in the electrolytes listed in Table 1, from pH −0.6 to 1. An almost linear dependence of exchange current density with pH in both sulfuric acid and perchloric acid is seen with a gradient of close to −0.4, very similar to the gradient of −0.5 presented by Bagotzky and Osetrova [1]. The derivation of the HOR/HER (Eqs. (9)–(20)) in terms of a Heyrovsky–Volmer reaction gives a dependence on hydrogen ion concentration, and that phenomenological dependence will depend on the precise values of the electrochemical rate constants (see below).

Durst et al. and Sheng et al. [31,32] also observed a reduction in exchange current density with pH and offered an alternative discussion linking it to a change in hydrogen binding energy (HBE) (proportional to the change in activation energy through the Bronsted–Evans–Polanyi relationship [33]). While a change in the Pt PZTC with pH was also considered (discussion on PZTC below), it has generally been found to decrease in potential with increasing pH [34], while here $E_{Peak,low}$ increases with pH; therefore it is unlikely to be the cause of this increasing $E_{Peak,low}$.

As will be shown below, the effect is adequately described by the full analysis of the Heyrovsky–Volmer model provided above.

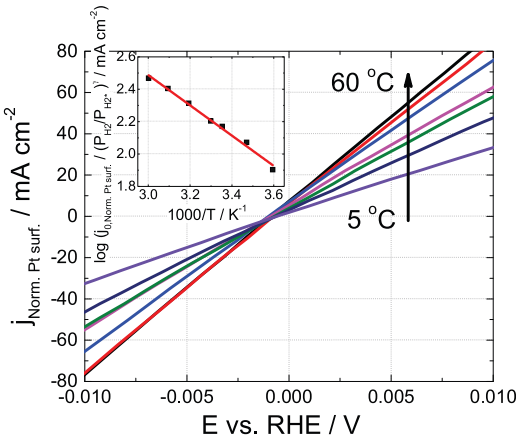

Fig. 6. Variation of *h*orwith temperature effects. 2.2 $\mu g_{Pt}\,cm^{-2}$HiSpec 9100 60 % Pt/C electrode in 4 mol $dm^{-3}HClO_4$, 1bar H_2, 10 mV s^{-1}, CE = Pt wire and RE = RHE. Inset shows an Arrhenius plot of j_0 after correction for increased water vapour partial pressure with temperature.

Table 2
"Raw" exchange current densities, and exchange current densities corrected by the hydrogen partial pressure variation due to the presence of water vapour for the HOR on HiSpec 9100 60 % Pt/C across a range of temperatures in 4 mol dm^{-3} $HClO_4$.

T/°C	5	15	25	30	40	50	60
$j_{0,T}$ /mA cm^{-2}	80	116	144	154	192	224	238
$j_{0,T}/\left(\frac{P_{H_2}}{P^{*}_{H_2}}\right)^{\gamma}$*/mA cm^{-2}	80	118	148	160	206	254	294

*exchange current density corrected for H_2O vapour partial pressure, $\gamma = 1$.

3.5. Exchange Current Density and Activation Energy

The micro-polarisation region of an anodic scan at different temperatures in 4 mol dm^{-3} $HClO_4$ is shown in Fig. 6. As the temperature increased, the gradient increased. Additionally, the scan cuts the x-axis at slightly negative potentials, which could be a sign of proton concentration varying with respect to the reference electrode, as discussed above. As each curve was scanned from the HER where protons will have been previously removed, the local pH will have shifted more alkaline. This shift of the local equilibrium potential by 0.7 mV equates to a local pH change of ~0.05 pH units. The cathodic scan also does not pass through the origin, but passes at a more positive potential, showing a more acidic local pH (results not shown). This effect cannot be accounted for by the capacitance of the electrode as the equivalent capacitive currents are about 20-fold smaller than the currents measured in the presence of hydrogen.

Due to the short potential range of the polarisation curve (±10 mV), linearization of the electrokinetic equations are possible and Eq. (19) (or Eq. (21) under suitable limiting conditions) can be used to calculate j_0 for each temperature, shown in Table 2. This requires the further assumption that through the potential range, the proton activity remains constant (i.e. proton concentration is not perturbed too much by the reaction). As this series of experiments were completed in the same electrolyte strength and the current densities are still relatively low, the proton activity is likely to remain relatively constant. The mass transport correction factor, which was present in [8], has been removed from Eq. (19) and (21) as; 1) with a peak current density of 600 mA cm^{-2}_{Spec} at 25 °C, the current was less than 10% at 10 mV over-potential and 2) the peak current density is assumed to be caused by a combination of the kinetics getting faster until an adsorption/local diffusion limiting current density was reached at larger over-potentials, and θ_{free} decreasing due to site blocking species, rather than a mass transport limitation; i.e., the geometric mass transport limitation is likely to be above this. The peak current density is discussed in detail in the Platinum PZTC section. The exchange current density at 25 °C is similar in both sulphuric and perchloric acid (see Fig. 5).

In Fig. 6 it can be seen that between 50 °C and 60 °C the rate of improvement in HOR performance with temperature decreases. This is due to reduced hydrogen partial pressure associated with increased water vapour partial pressure. To correct for this, the gas phase in the catalyst layer and down the pores of the polycarbonate track etched membrane was assumed to be at equilibrium with the saturation vapour pressure of water for that corresponding temperature. This is very plausible considering the catalyst layer is in contact with an aqueous electrolyte. The effect is corrected for in the third row in Table 2 assuming a hydrogen reaction exponent, γ, of unity, as discussed in the hydrogen partial pressure measurements above.

Using the Arrhenius equation, adapted for the exchange current density with water vapour and hydrogen partial pressure correction (Eq. (23)), the activity can be plotted vs. the inverse temperature as in the inset in Fig. 6, giving the gradient as the activation energy at 18 kJ mol^{-1}.

$$E_a = -2.303R\frac{\Delta \log\left(j_0 / \left(\frac{P_{H_2}}{P^{*}_{H_2}}\right)^{\gamma}\right)}{\Delta 1/T} \quad (24)$$

The rate constant (k_0^{eq}) can be related to the exchange current density by normalising to standard conditions. Due to the additional observed change in exchange current density by proton activity for acidic conditions, Eq. (21) relates the exchange current density through activation energy (E_a) at 25 °C, partial pressure fraction of 1 and pH 0.

3.5.1. Full fit of experimental data set

Recent developments in measuring the HOR and HER at high mass transports have promoted a number of attempts to model the hydrogen oxidation and evolution reaction in the literature. For instance Chen and Kucernak [8] considered whether Tafel–Volmer or Heyrovski–Volmer kinetics adequately explained single Pt particle microelectrode results whereas others [35–37] have considered a potential dependent switch from Tafel–Volmer to Heyrovski–Volmer kinetics. While both models can fit the mass transport limited curve from the RDE and the shoulder in the curve observed by Chen and Kucernak [8], both models in their current forms are not capable of predicting the double peak with a dip in current in-between as observed here and in other papers [12,17]. Clearly from the results above, there is also a significant anion surface blocking effect and pH effect which controls the electrokinetics of the HOR and any model which is going to reproduce the experimental curves needs to include these effects. To outline some of the elements needed for such a model, the potential of zero total charge and potential dependence of anion adsorption are discussed below.

However, for the HOR or HER on the anode of a fuel cell or the cathode of an electrolyser, the over-potential typically remains below 10 mV. Therefore, in this paper we provide two different numerical fits to all the data presented across a polarisation range of ±10 mV and a variety of experimental conditions. We also show that these models may be extended to about ±50 mV without introduction of too much error. Such numerical fits may be useful in providing models for fuel cell anodes and electrolyser cathodes. The fits utilise either Eq. (19) or (21). Fits utilising the latter approximate the approaches previously used in the literature in which it is assumed that the concentration dependence of protons and hydrogen can be separated from an extrinsic rate constant, whereas the fit utilising Eq. (19) is the full explicit Heyrovsky–Volmer approach. In both cases the potential was corrected for the small shift in pH which led to the scan not passing through the origin (shift <1 mV in all cases). The fitting parameters when using Eq. (19) were $K, k_1^{eq}, k_2^{eq}, E_a$. In this case there are no stoichiometric coefficients for protons and hydrogen as their activity is included explicitly within the kinetic equation. An "effective" stoichiometric coefficient may be calculated by examining how the exchange current density calculated from the fitted parameters varies as a function of the reactant concentration within the appropriate concentration range. The fitting parameters when using Eq. (21) were k_0^{eq}, E_a, ε and γ. Both fits were performed on all datasets simultaneously (20 data sets). The operating conditions for the datasets are described in a footnote to Table 3.

The specific current density ($j_{Norm.Ptsurf.}$) can be converted to absolute current (i), geometric current density (j_{Geo}) or mass activity (j_{Mass}) through Eq. (25).

$$i = j_{\text{Norm.Pt surf.}} \times A \times SA_{Pt} \times L_{Pt} = j_{Geo} \times A = j_{Mass} \times A \times L_{Pt} \quad (25)$$

These terms are linked through the electrode area (A), the platinum loading (L_{Pt}) and the catalyst's metal area (SA_{Pt}). The

Table 3
Summary of values experimentally measured in this paper under standard conditions, $a_{H^+} = 1$; $a_{H2} = 1$; T = 298 K. Global fits were determined by simultaneously fitting 20 data sets using either Eq. (21) (Global Fit 1) or Eq. (19) (Global fit 2). Hydrogen partial pressures were corrected for water vapour. Grey cells denote the parameters used in the fitting process.

	Description	Observed	Global Fit 1[a]	Global Fit 2[b]
$k_{0,obs}{}^{eq}$/cm s^{-1}	Rate constant		0.86[c]	n.a.
K	Ratio of forward and reverse rate constants		n.a.	2.6
$k_1{}^{eq}$/mol cm^{-2} s^{-1}	Rate constant		n.a.	1.79×10^{-6}[d]
$k_2{}^{eq}$/mol cm^{-2} s^{-1}	Rate constant		n.a.	1.19×10^{-6}
E_a/kJ mol^{-1}	Activation energy	18[e]	15.4	15.5
$j_{0,298K}$/mA cm$^{-2}{}_{Spec}$	Exchange current density		86	101[f]
γ	Hydrogen activity reaction order	0.68[g]	0.44	0.62[h]
ε	Proton activity reaction order	0.4[i]	0.36	0.38[j]

Datasets simultaneously fitted:
T = 298K, c_{H+} = 0.5 M $HClO_4$, p(H_2) = 101,13,11,9,7,5,3,1 kPa.
c_{H+} = 4 M $HClO_4$, p(H_2) = 101 kPa, T = 278,288,298,303,313,323,333 K.
T = 298K, p(H_2) = 101 kPa, c_{H+} = 0.1,0.25,0.63,1.59,4.0 M $HClO_4$.
[a] using Eq. (21);
[b] using Eq. (19);
[c] calculated from exchange current density assuming Eq. (21);
[d] If we do not use activities in the derivation of equation (21), then this parameter is 3.51 cm s^{-1} based on a saturated hydrogen concentration of 5.1×10^{-7} mol cm^{-3};
[e] from slope of Fig. 6 (inset);
[f] using Eq. (21) and fitted values of K, $k_1{}^{eq}$, $k_2{}^{eq}$;
[g] Slope of Fig. 2(b) at 10 mV overpotential;
[h] intrinsic value is 1, but estimated from $\left(\frac{\partial \log(j_o)}{\partial \log(p_{H_2})}\right)_{p_{H_2}=p^\ominus}$;
[i] Slope of Fig. 5;
[j] intrinsic value is 1, but estimated from $-\left(\frac{\partial \log(j_o)}{\partial pH}\right)_{pH=0}$.

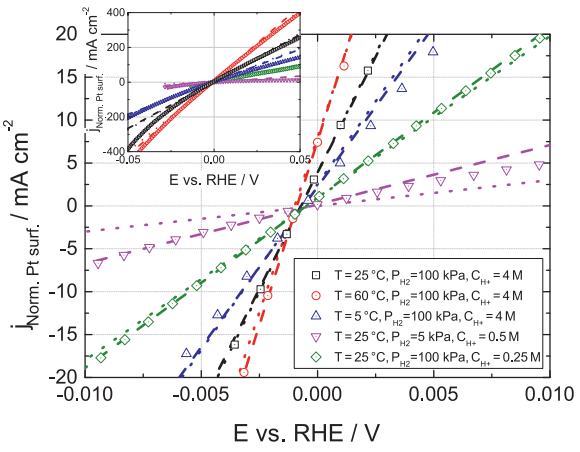

Fig. 7. Data (points) and associated fits to Eq. (19) (.....), and Eq. (21) (———) at low over-potentials under different conditions See text for further details of fits.

values for the fit are presented in right most columns in Table 3, with a selection of results which represent the dataset shown with their corresponding fits in Fig. 7. For all the curves, and both fitting approaches, with $\eta \leq 10$ mV for the *hor*, the least squares error for fitting is within 15%. These fits also continues to predict the HOR behaviour fairly well up to ±50 mV overpotential, however, the HER seems to be slightly under estimated at higher overpotentials.

Both fitting functions produce similar goodness of fit, and also show similar values of activation energy (the only parameter common to both fits), with a value a little less than the value determined solely by fitting the data in Fig. 6.

For the fit derived from the simplified analysis based on Eq. (21), Fit 1, it can be seen that the hydrogen concentration reaction order (γ), deviates somewhat from the value determined from independently fitting the data at an overpotential of 10 mV. In contrast, the value for the proton activity reaction order is close to the value obtained by individually fitting each parameter. An exchange current density under standard conditions of 86 mA cm^{-2} is fit. However, no further insight is gained into the mechanistic reason for the values of the apparent reaction orders.

For the fit based on linearization of the exact Heyrovsky–Volmer equation (Fit 2), Eq. (19), the value of K implies that under standard conditions the equilibrium value of the forward Volmer rate constant is only slightly faster than the reverse Volmer step, suggesting discharge of protons on the platinum surface is similar to the rate of adsorbed hydrogen atom oxidation. The values of the rate constants for $k_1{}^{eq}$ and $k_2{}^{eq}$ are rather close to each other in numerical value. The calculated exchange current density under equilibrium conditions, at 101 mA cm^{-2} is derived from K, $k_1{}^{eq}$ and $k_2{}^{eq}$ (Eq. (19)). It is important to note that as conditions are changed away from equilibrium conditions, j_o will vary in a complex way with pH and hydrogen concentration, as shown below. Although the derivation of the Heyrovsky–Volmer equation implicitly assumes a reaction order of one for protons and hydrogen within the individual micro-steps of Eqs. (6) & (7), a non-unity reaction order may occur due to the interaction of the reactant activities within Eqs. (16) and (17) and its linearised form (19). As discussed previously, we would expect Eq. (21) to only be applicable under certain conditions, notably $Kk_1^{eq}a_{H_2}surf \gg k_2^{eq}$ or $Kk_1^{eq}a_{H_2\,surf} \ll k_2^{eq}$ and K>>1 or K<<1. Comparison with the fitted values of the parameters shows that although $K >> 1$, $Kk_1^{eq}a_{H_2\,surf} \approx k_2^{eq}$ when $a_{H_2\,surf}$ is equivalent to the value achievable with 1 bar hydrogen. Hence we would not expect that we can apply Eq. (21) to the experiments we have performed.

To better probe the phenomenological reaction orders, we have looked at the sensitivity of the exchange current under standard conditions

$$\gamma = \frac{\mathrm{d}\log(j_0)}{\mathrm{d}\log(P_{H_2})} \quad \varepsilon = \frac{\mathrm{d}\log(j_0)}{\mathrm{d}\log(a_{H^+})} \tag{26}$$

In Fig. 8 we provide double logarithmic plots of the exchange current versus the reactant concentrations using the fitting parameters in Table 3 to calculate the exchange current as a function of reactant concentration using equation (19). As expected from the previous discussion, we see that the exchange current density does not show a linear response with reactant concentration showing that we are in the regime where the reaction orders cannot be easily separated out from the exchange

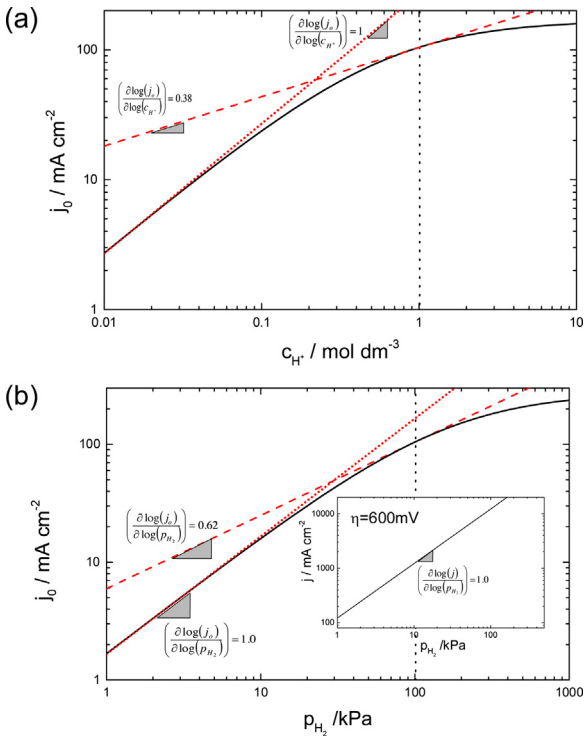

Fig. 8. Plots of sensitivity of effective exchange current density as a function of (a) acid concentration; and (b) hydrogen partial pressure calculated using Eq. (19). The dashed lines (———) are the tangents at c(H^+) = 1.0 mol dm^{-3} and p_{H2} = 101 kPa representing the phenomenological reactant order under those conditions. The dotted lines (.....) represent the limiting behaviour where the phenomenological reaction orders are one. Inset in (b) is the current density versus hydrogen partial pressure plot calculated at an overpotential of 0.6 V. T = 298 K; K = 2.6, k_1^{eq} = 1.79 × 10^{-6} mol cm^{-2} s^{-1}, k_2^{eq} = 1.19 × 10^{-6} mol cm s^{-1}, T = 298 K, p_{H2} = 101 kPa (except in (b)), c(H^+) = 1.0 mol dm^{-3} (except in (a)).

current as was performed in Eq. (21). We only see this occurring when the pH > 1 or when p_{H2} < 10 kPa. Under standard conditions, we can extract the effective reactant stoichiometries by determining the tangents of the curves at the standard conditions. We find that for both hydrogen and protons, the effective values of γ and ε are very close to those determined from the data, Table 3. Furthermore, inset within Fig. 8(b) we also plot the variation of current density with hydrogen partial pressure under standard conditions, and at an overpotential of 0.6 V, equivalent to the experimental result in Fig. 2(b). The reaction order we obtain from this plot is 1.0, in good agreement with the experimental results. Taking all the fitting results, and the ability to well describe the reaction order phenomena, it would appear that the full Heyrovsky–Volmer model provides a good explanation for the experimental data.

3.5.2. Comparison to the literature

Due to the varying experimental conditions in the literature it is hard to give an exact comparison to the values of j_0, however, Table 4 presents some j_0 values mostly at room temperature. Looking across the pH range as presented in Table 1, Bagotzky and Osetrova's [1] achieved a similar exchange current density as presented in this paper with j_0 > 50 mA cm$^{-2}{}_{Spec}$ in the same acid concentration of 1 mol dm^{-3}, while Durst et al. [31] measured j_0 = 200 mA cm$^{-2}{}_{Spec}$ in a high mass transport hydrogen pump configuration (reported at pH 0) although at the slightly raised temperature of 30 °C. At 0.1 mol dm^{-3} acid strength, an exchange current density of 32 mA cm$^{-2}{}_{Spec}$ is close to previous results in this group [8] and Sun et al. [10] at 24 and 27 mA cm$^{-2}{}_{Spec}$, respectively (note: these results would be 48 and 54 mA cm$^{-2}{}_{Spec}$ when calculated through Eq. (21)).

Values outside the measured pH range in this paper include Zhou et al. [5] and Zoski [6], obtaining j_0's of 60–80 and 42 mA cm$^{-2}{}_{Spec}$ for 0.01 mol dm^{-3} perchloric acid and Vogel et al. obtaining 18–27 mA cm$^{-2}{}_{Spec}$ at a higher acid concentration of 96% H_3PO_4. While these values are comparable to values reported here, if extrapolated to comparable acid strengths, they would be somewhat different.

A number of literature sources also presented much lower values of <2 mA cm$^{-2}{}_{Spec}$ for example [3,4,7,9], which are still low if corrected for acid strength. The much lower exchange current densities are likely to either have not been fully corrected for mass transport effects, or suffer from a reduced utilisation of catalyst due to a hydrogen diffusion gradient through the catalyst layer [10]. For example, Song et al. [9] reported an exchange current density of 1.73 mA cm$^{-2}{}_{Spec}$ while testing in a PEFC with a catalyst loading of 1 mg$_{Pt}$ cm^{-2} between their anode and cathode. The high activity of the HOR on Pt is likely to cause hydrogen depletion through the catalyst layer leaving a high percentage of catalyst sites to remain inactive. Only by using an ultra-thin catalyst layer

Table 4
A comparison of literature obtained exchange current densities and activation energies, T close to 298 K.

Technique	Conditions	j_0/mA cm^{-2}	Ea/kJ mol^{-1}	Reference
Floating electrode (Pt/C) Fit 1	1 mol dm^{-3} $HClO_4$, 25 °C	86	15.4	This Work
Floating electrode (Pt/C) Fit 2	1 mol dm^{-3} $HClO_4$, 25 °C	101	15.5	This Work
Pt microelectrode with a thin film of electrolyte	0.5–1 mol dm^{-3} H_2SO_4, r.t	> 50	–	[1]
Rapid potentiodynamic scanning polycrystalline Pt, Pt black, Pt/C	96% H_3PO_4, 22 °C	27,21,18	10.5	[2]
RDE (single crystal: 110, 100, 111)	0.05 mol dm^{-3} H_2SO_4, 30 °C	0.98, 0.60, 0.45	9.5, 12, 18	[3]
RDE (Pt disk) with and without a Nafion film	0.1 mol dm^{-3} $HClO_4$, r.t.	1.62, 1.35	–	[4]
Pt microelectrode SECM	0.01 mol dm^{-3} $HClO_4$ + 0.1 mol dm^{-3} $NaClO_4$, r.t.	60 - 80	–	[5]
Pt microelectrode SECM	0.01 mol dm^{-3} $HClO_4$ + 0.1 mol dm^{-3} $NaClO_4$, r.t.	~42	–	[6]
RDE (PtRu/C and Pt/C)	0.5 mol dm^{-3} H_2SO_4, 25 °C	1 - 2	–	[7]
Single particle microelectrode	0.1 mol dm^{-3} H_2SO_4, 23 °C	24†	–	[8]
Fuel cell (calculated from V_{loss} for different anode loadings)	Nafion® 112, 60 °C	27	–	[43]
Hydrogen pump (Pt/C)	≤800 EW, 80 °C ≤800 EW, 30 °C	235 – 300† 100†	–	[16]
Fuel cell (PtRu/C)	Nafion® 112, 23 °C, 304 kPa H_2	1.73	34.6	[9]
RDE (low loading Pt/C)	0.1 mol dm^{-3} $HClO_4$, 25 °C	27†	43	[10]
Fuel cell (sputtered Pt)	Nafion 115, 80 °C	770†	–	[17]
Fuel cell (nanostructured thin film PtCoMn)	850 EW (3M), 80 °C	489 (42*)	38.9	[11]

SECM = scanning electrochemical microscope, r.t. = room temperature.
* Extrapolated to 25 °C for the given activation energy.
† Exchange current density calculated using j = 2F/RT(j_0), not j = F/RT(j_0), giving factor of 2 lower values than would be reported through Eq. (21).

can all the catalyst be assured to be well supplied with hydrogen and therefore fully active.

Table 4 also shows activation energies quoted in the literature; scattered between 10–43 kJ mol^{-1}, with the value reported here lying between these values. This medium activation energy means that the exchange current density is less affected by temperature then recently reported values [9–11]. Extrapolating the exchange current density for an acid concentration range of 1–4 mol dm^{-3} to a more typical operating temperature of a fuel cell at 80 °C gives a range of 260–440 mA cm$^{-2}{}_{Spec}$. This range is close 470–600 mA cm$^{-2}{}_{Spec}$ reported by Neyerlin et al. [16] (using their equation with $\alpha_a + \alpha_b = 1$ which is in the same form as Eq. (21)), 489 mA cm$^{-2}{}_{Spec}$ reported by Wang et al. [11] and 405 mA cm$^{-2}{}_{Spec}$ by extrapolating the exchange current density at 25 °C from Sun et al. [10] using their activation energy. However it is much lower than the 770 mA cm$^{-2}{}_{Spec}$ reported by Wesselmark et al. [17]. Note that Sun et al. and Wesselmark et al. have a factor of two difference due to the method of calculation, which would make their values larger than those reported here. This still leaves a large variation in exchange current densities reported at both low (20 °C) and high (80 °C) temperature, however, with the introductions of higher mass transport techniques, higher exchange current densities are generally being reported. Also, while most results have a comparable catalyst as used here (Pt/C), others used different catalysts such as a nanostructured thin film PtCoMn [11] and a sputtered Pt layer catalyst [17] and therefore the activities could be substantially different. This still leaves a large variation in exchange current densities reported at both low (20 °C) and high (80 °C) temperature, however, with the introductions of higher mass transport techniques, higher exchange current densities are generally being reported.

3.6. Platinum PZTC

As discussed above, the HOR curve was not affected by anion species below $E_{Peak,low}$, while above $E_{Peak,low}$, a large anion affect was observed. The adsorption of anion (and cation) species are strongly dependent on the charge at the surface of the electrode (Pt in this case). The potential of zero free charge (PZFC) is a commonly used potential where the surface of the electrode has a zero total charge, first postulated by Frumkin and Petrii [38], and is generally measured in ultra-high vacuum. In an electrolyte, the ions in the solution interact with the surface, and therefore the PZFC cannot be measured. Instead, a potential of zero total charge (PZTC) can be measured which is the potential where the total charge at the electrode surface plus the charge density transferred during the adsorption process equals zero [19,20,38]. Due to the interaction with the electrolyte, different electrolytes or electrolyte concentrations cannot directly be compared, but only used as a guide.

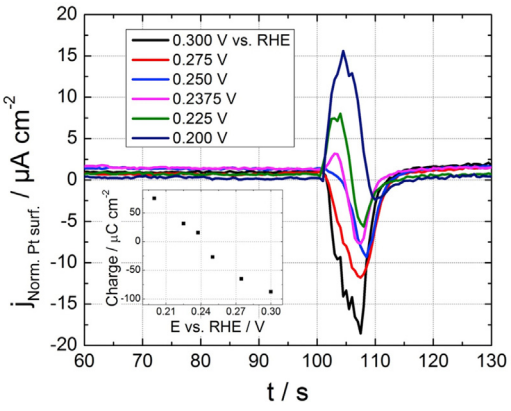

Fig. 9. Current measured from CO displacement on 2.4 nm Pt nanoparticles supported on carbon in 4 mol dm^{-3} $HClO_4$ at 298 K. CE = Pt wire, RE = RHE. The inset shows the charge density with respect to potential, with the PZTC at 0.24 ± 0.01 V vs. RHE (intercept of the x-axis).

Fig. 9 shows the resultant current flow from CO displacement of the adsorbed species on the HiSpec 9100 Pt/C with a particle size of 2.4 nm [18] coated in Nafion at different potentials in 4 mol dm^{-3} perchloric acid. The noise in the graph occurs as the electrode is floating on the electrolyte surface and is slightly disrupted by the purge of nitrogen or CO; which in this case is bubbled through the solution. As the potential increases, the charge associated with the displacement current moves from a positive to a negative current, showing a shift in adsorbed species from cations to anions, inset in Fig. 9. The x-intercept shows the PZTC is 0.24 ± 0.01 V vs. RHE. This value is shifted negative in comparison to the PZTC of polycrystalline platinum at 0.285 V vs. RHE in 0.1 mol dm^{-3} $HClO_4$ [20]. However, studies on single crystals [19] have shown that the PZTC of polycrystalline Pt is an average of the surface facets; Pt(1 1 0), Pt (1 1 1) and Pt(1 0 0); in 0.1 mol dm^{-3} $HClO_4$ they are 0.23, 0.34 and 0.43 V vs. RHE, respectively. With the particle size of 2.4 nm, a cuboctahedron particle would contain Pt(1 0 0) and Pt(1 1 1) facets; however, this would not account for the decrease in PZTC to 0.24 V vs. RHE. Climent et al. [39,40] showed that an increased fraction of step density to surface facets caused a negative shift in PZTC and therefore these step sites have a lower PZTC (they measured a Pt (1 1 0) step to have a PZTC of ~0.15 V vs. RHE). Mayrhofer et al. [20] applied this to nano-particles, showing that as the particle size decreased (or ratio of edges to facets increases), the PZTC shifted negative in potential. Our PZTC value is close to Mayrhofer et al.'s value reported for a 1 nm Pt particle size under a thin film of Nafion and in 0.1 mol dm^{-3} $HClO_4$; while both catalyst layers are bound with Nafion, the use of different electrolyte concentrations make the results not directly comparable, as discussed above.

Comparing the PZTC to the HOR in Fig. 1, it could be expected that the decrease in current density coincides with the adsorption of anions acting as site blocking species, reducing the active Pt surface area (assuming that the rate limiting step is the adsorption of hydrogen and therefore site dependent). However, the measured PZTC falls between the potentials of the two peaks. This suggests that the two peaks in the HOR are two different sites (edges and facets) with different PZTC's and the measured PZTC corresponds to the ratio of the two respective sites (as for polycrystalline Pt with its different facets). As the step density has been shown to lower the PZTC, this suggests the edge sites would have a PZTC below 0.24 V vs. RHE, and we propose that this is where $E_{Peak,low}$ appears at 0.2 V vs. RHE. While the facets would be made of Pt(1 0 0) and Pt (1 1 1) facets and in 0.1 mol dm^{-3} $HClO_4$ they have a PZTC of 0.34 and 0.43 V vs. RHE, and we propose this is where $E_{peak,high}$ sits at 0.36 V vs. RHE. Therefore, below the PZTC for the respective surface site, H_{ads} is the dominant surface adsorbed species and the HOR increases with over-potential. This is supported by the fact that there is no effect of anion species below $E_{Peak,low}$ in Fig. 3. Above the PZTC of the respective surface, the onset of competitively adsorbing anions hinders the reaction, causing a current decay. This implies that the ratio of the peak heights would change with facets to edge ratio or particle size; the authors are currently exploring this hypothesis.

While the two peaks in Fig. 1 have been observed on Pt elsewhere [17] in high mass transport techniques, the decay in mass transport above $E_{Peak,high}$ has not been widely presented at such low potentials, typically because the HOR remains under mass transport limitations until high potentials are exceeded. The current decay has mainly been studied using the RDE, occurring at >0.8 V vs. RHE and rationalised by the formation of oxides. However, as the current is mass transport limited on the RDE between 0.1–0.8 V vs. RHE, the potential at which the current

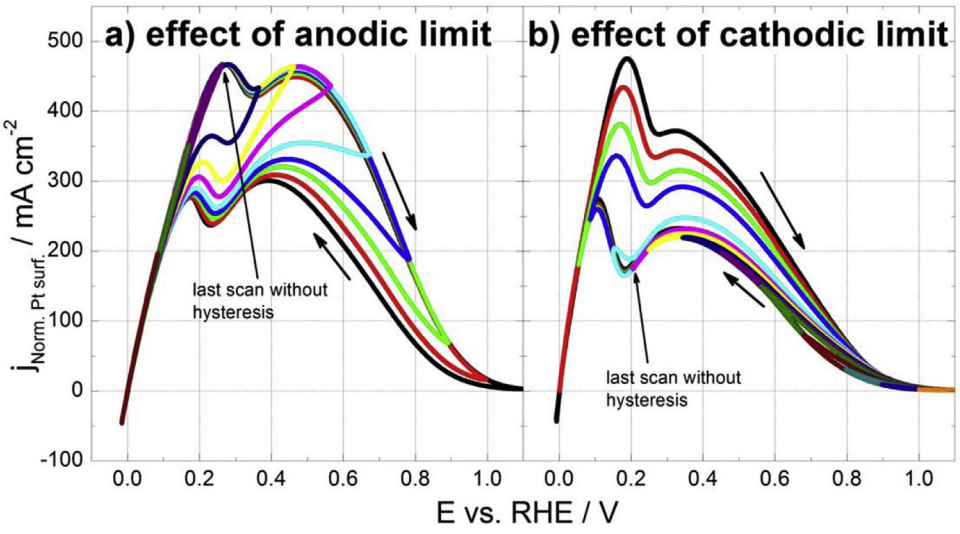

Fig.10. Effect of scan limit on two Pt/C electrodes: a) shows the change in anodic limit with a 0.7 $\mu g_P\,cm^{-2}$ electrode in 0.5 mol dm^{-3} $HClO_4$ and b) shows the change in cathodic limit with a 1.9 $\mu g_{Pt}\,cm^{-2}$ electrode in 4 mol dm^{-3} $HClO_4$. Both run with the conditions H_2, 298 K, 10 mV s^{-1}, CE = Pt wire and RE = RHE.

begins to decay is masked. In fact, the decay in current in our results above 0.8 V vs. RHE in Fig. 1 is very similar to the decay in current density seen in the RDE once $j < j_{MT}$ (this can be seen clearly in the inset of Fig. 9 in [12]).

A suitable comparison of the HOR can be made with Ru in the RDE. Due to its order of magnitude lower activity, this reaction can be measured without becoming mass transport limited. In Fig. 2 of [41], a broad peak was observed at ~0.2 V vs. RHE and attributed to a kinetic limitation in agreement with the discussion here for Pt. A single peak was observed, but as they were using polycrystalline Ru, the edge contribution is likely to be minimal. After the peak current density, the current decayed rapidly to almost zero at 0.4 V vs. RHE. The authors assigned this decay to oxide adsorption, with Ru well known to have an onset of oxide formation at low potentials which assists in the oxidation of carbonaceous species (e.g. CO). This decay is very similar in shape to the decay observed for Pt here, where the current density decays 5 fold from ~500 mA $cm^{-2}{}_{Spec}$ at 0.2 V to <100 mA $cm^{-2}{}_{Spec}$ at 0.8 V in Fig. 1. As described above, on platinum we ascribe this decay to anion adsorption (sulfonate chains of the PFSI and perchlorate ions) as oxide formation is not considered to occur until higher potentials, and the onset of the current decay seems to be coincident with the PZTC. For the case of Ru however, specifying whether anion adsorption or oxide species dominate in the decay is challenging, and is likely to be a mixture of both.

3.7. Hysteresis of the HOR

Fig. 10 shows the effect of a) the anodic limit and b) the cathodic limit on two window opening scans for the HOR. The precise shape of the curves in the two window opening experiments is slightly different, due to the effect of electrolyte concentration as discussed above, with Fig. 10a) and b) run in 0.5 and 4 mol dm^{-3} perchloric acid, respectively. The anodic scan limit shows a "humming bird" shape, where the scan starts at −0.01 V vs. RHE for all scans and the upper limit changes from 0.1 to 1.1 V vs. RHE. The last scan without hysteresis (labelled) has an upper potential of 0.22 V vs. RHE for this CV and is just before $E_{Peak,low}$. The next scan, with upper potential of 0.33 V vs. RHE, displays a hysteresis loop. As discussed in the Platinum PZTC section, after $E_{Peak,low}$, anion adsorption occurs on the Pt edge sites, reducing the current density. In addition, the current density carries on decreasing as the potential is reversed and only when the potential goes below the PZTC again, does the current density start to recover. As the upper potential limit increases further, the hysteresis increases (i.e. current on the cathodic scan decreases), possibly showing that this anion adsorption proceeds on the surface as the potential is increased. This has the effect of blocking the HOR, and remains on the surface until the potential is scanned below the PZTC for the specific site. At higher potentials, this anion adsorption will change to oxide formation, further perturbing the HOR.

For the cathodic scan limit window opening experiment (Fig. 10b), the scans start at 1.1 V vs. RHE and the lower scan limit reduces in potential from 1 to −0.1 V vs. RHE. The scans between 1.1 V vs. RHE and $E_{Peak,low}$ all show little hysteresis, with the last scan showing no hysteresis labelled. There is a slight hysteresis in the high potential region (0.6–0.9 V), and this seems to be associated with oxide formation and reduction. Therefore, a consistent behaviour is observed for the site blocking species perturbing the current density down to a potential of 0.2 V. However, all of these scans follow the lower cathodic scan, suggesting that a percentage of the sites remain irreversibly blocked and only when the potential decreases to $E_{Peak,low}$ (or the PZTC of the edges), do these sites become re-activated. This is shown by the gradual increase in current density (and hysteresis) of the anodic scan as the lower potential limit moves from $E_{Peak,low}$ to −0.1 V vs. RHE; only upon going below 0 V vs. RHE does the current density fully recover to j_{Max}. This partial deactivation of the HOR occurs across the entire potential region of the ORR, and it is intriguing to consider whether the HOR could be used as a probe for the state of the Pt surface during the ORR.

4. Conclusion

Using the floating electrode technique, kinetic parameters have been extracted from the HOR with no mass transport correction factor. This is made possible through a mixture of the high mass transport capability and an optimised low loading catalyst layer. The high mass transport capability has enabled rapid gas transport towards the catalyst layer (HOR) or away from the catalyst layer (HER). Maximum current densities of 0.6 and 8 A $cm^{-2}{}_{Spec}$ which corresponds to 1200 and 19,000 H_2 molecules per surface platinum atom per second were observed for the HOR and HER, respectively. The low catalyst loading enables homogeneous conditions across

the catalyst layer (removing internal polarisation gradients), allowing definition such as the two peaks observed in the HOR.

For both perchloric and sulphuric acid, negligible anion effect was seen for the HOR below $E_{Peak,low}$. These potentials are below the PZTC where little anions adsorption is expected and therefore we conclude the exchange current density can be measured in either perchloric or sulphuric acid (for a set pH). Above $E_{Peak,low}$, a > 5 fold decrease in activity occurred between 0.2 and 0.8 V vs. RHE (before the onset of oxide formation), showing anion adsorption perturbates the reaction. While the Pt/Nafion/perchloric acid environment had a 5 fold decrease, the Pt/Nafion/sulphuric acid had a 10 fold decrease, showing the stronger adsorbing sulfuric acid has a greater blocking effect.

Our data suggests that proton generation during the HOR cannot be ignored as it was found to cause a shift in the local pH towards higher current densities (causing $E_{peak,low}$ to shift to positive potentials) and the pH of the acid was found to alterthe exchange current density (in the pH range studied).

We have developed and analytically solved the full Heyrovsky-Volmer equation and find that it adequately explains our experimental results in that

a) It correctly predicts the effective reaction order for protons and hydrogen under standard conditions;
b) it correctly predicts the reaction order at high over potentials
c) it is capable of replicating electrochemical performance in a dataset comprising of almost three orders of magnitude of hydrogen partial pressure; more than an order order of magnitude of hydrogen concentration and a temperature range from 278–333 K.

The linearised form of the model may be of significant relevance to fuel cells and electrolysers. A further improvement to this work would be to derive a model to fit the HOR across the entire potential region. To do this, understanding of the anion effects at high potential are needed. Furthermore, this model should be considered for studying hydrogen oxidation under alkaline conditions.

In addition, we have presented evidence that the two peaks correspond to two different surface sites, edges or Pt atoms with low coordination numbers ($E_{Peak,low}$) and facets ($E_{Peak,high}$) and that the experimentally measured PZTC is a contribution of the two. Further work is currently been completed with different Pt particle sizes (changing the ratio of edges to facets) to explore the change in the ratio of the peak heights.

Acknowledgements

The authors would like to thank the U.K. Engineering and Physical Sciences Research Council (EPSRC) for funding through Hydrogen to Fuel Cells (H2FC SUPERGEN) Flexible Funding Award EPSRC Grant Ref. EP/J016454/1; EP/G030995/1 – Supergen Fuel Cell Consortium – Fuel cells – Powering a Greener Future – CORE; and EP/K503733/1 – EPSRC Impact Acceleration Research Grant.

References

[1] V.S. Bagotzky, N.V. Osetrova, Investigations of hydrogen ionization on platinum with the help of micro-electrodes, Journal of Electroanalytical Chemistry and Interfacial Electrochemistry 43 (1973) 233–249.
[2] W. Vogel, L. Lundquist, P. Ross, P. Stonehart, Reaction pathways and poisons—II: The rate controlling step for electrochemical oxidation of hydrogen on Pt in acid and poisoning of the reaction by CO, Electrochim. Acta 20 (1975) 79–93.
[3] N.M. Marković, B.N. Grgur, P.N. Ross, Temperature-Dependent Hydrogen Electrochemistry on Platinum Low-Index Single-Crystal Surfaces in Acid Solutions, The Journal of Physical Chemistry B 101 (1997) 5405–5413.
[4] J. Maruyama, M. Inaba, K. Katakura, Z. Ogumi, Z.-i. Takehara, Influence of Nafion® film on the kinetics of anodic hydrogen oxidation, Journal of Electroanalytical Chemistry 447 (1998) 201–209.
[5] J. Zhou, Y. Zu, A.J. Bard, Scanning electrochemical microscopy: Part 39. The proton/hydrogen mediator system and its application to the study of the electrocatalysis of hydrogen oxidation, Journal of Electroanalytical Chemistry 491 (2000) 22–29.
[6] C.G. Zoski, Scanning Electrochemical Microscopy: Investigation of Hydrogen Oxidation at Polycrystalline Noble Metal Electrodes, The Journal of Physical Chemistry B 107 (2003) 6401–6405.
[7] J.X. Wang, S.R. Brankovic, Y. Zhu, J.C. Hanson, R.R. Adžić, Kinetic Characterization of PtRu Fuel Cell Anode Catalysts Made by Spontaneous Pt Deposition on Ru Nanoparticles, Journal of The Electrochemical Society 150 (2003) A1108–A1117.
[8] S. Chen, A. Kucernak, Electrocatalysis under Conditions of High Mass Transport: Investigation of Hydrogen Oxidation on Single Submicron Pt Particles Supported on Carbon, The Journal of Physical Chemistry B 108 (2004) 13984–13994.
[9] C. Song, Y. Tang, J.L. Zhang, J. Zhang, H. Wang, J. Shen, S. McDermid, J. Li, P. Kozak, PEM fuel cell reaction kinetics in the temperature range of 23–120 °C, Electrochimica Acta 52 (2007) 2552–2561.
[10] Y. Sun, J. Lu, L. Zhuang, Rational determination of exchange current density for hydrogen electrode reactions at carbon-supported Pt catalysts, Electrochim. Acta 55 (2010) 844–850.
[11] X. Wang, R.K. Ahluwalia, A.J. Steinbach, Kinetics of Hydrogen Oxidation and Hydrogen Evolution Reactions on Nanostructured Thin-Film Platinum Alloy Catalyst, Journal of The Electrochemical Society 160 (2013) F251–F261.
[12] C.M. Zalitis, D. Kramer, A.R. Kucernak, Electrocatalytic performance of fuel cell reactions at low catalyst loading and high mass transport, Physical Chemistry Chemical Physics 15 (2013) 4329–4340.
[13] J. Jiang, A. Kucernak, Investigations of fuel cell reactions at the composite microelectrode|solid polymer electrolyte interface. I. Hydrogen oxidation at the nanostructured Pt|NafionÂ® membrane interface, J. Electroanal. Chem. 567 (2004) 123–137.
[14] T.A. Greszler, D. Caulk, P. Sinha, The Impact of Platinum Loading on Oxygen Transport Resistance, Journal of The Electrochemical Society 159 (2012) F831–F840.
[15] C.M. Zalitis, D. Kramer, J. Sharman, E. Wright, A.R. Kucernak, Pt Nano-Particle Performance for PEFC Reactions at Low Catalyst Loading and High Reactant Mass Transport, ECS Transactions 58 (2013) 39–47.
[16] K.C. Neyerlin, W. Gu, J. Jorne, H.A. Gasteiger, Study of the Exchange Current Density for the Hydrogen Oxidation and Evolution Reactions, Journal of The Electrochemical Society 154 (2007) B631–B635.
[17] M. Wesselmark, B. Wickman, C. Lagergren, G. Lindbergh, Hydrogen oxidation reaction on thin platinum electrodes in the polymer electrolyte fuel cell, Electrochem. Commun. 12 (2010) 1585–1588.
[18] Certificate of Analysis, Correspondence with Johnson Matthey Fuel Cells, 16 Dec 2009.
[19] V. Climent, R. Gomez, J.M. Orts, A. Rodes, A. Aldaz, J.M. Feliu, Electrochemistry, Spectroscopy, and Scanning Tunneling Microscopy Images of Small Single-Crystal Electrodes, in: A. Wieckowski (Ed.), Interfacial Electrochemistry Theory, Experimental, and Application, MarcelDekker, Inc., New York, 1999, pp. 463.
[20] K.J.J. Mayrhofer, B.B. Blizanac, M. Arenz, V.R. Stamenkovic, P.N. Ross, N.M. Markovic, The Impact of Geometric and Surface Electronic Properties of Pt-Catalysts on the Particle Size Effect in Electrocatalysis, The Journal of Physical Chemistry B 109 (2005) 14433–14440.
[21] C.M. Zalitis, A.R. Kucernak, Manuscript in preparation.
[22] K.L. Hsueh, E.R. Gonzalez, S. Srinivasan, Electrolyte effects on oxygen reduction kinetics at platinum: A rotating ring-disc electrode analysis, Electrochimica Acta 28 (1983) 691–697.
[23] R. Subbaraman, D. Strmcnik, V. Stamenkovic, N.M. Markovic, Three Phase Interfaces at Electrified Metal-Solid Electrolyte Systems 1. Study of the Pt(hkl)-Nafion Interface, The Journal of Physical Chemistry C 114 (2010) 8414–8422.
[24] M.S. Rau, M.R. Gennero de Chialvo, A.C. Chialvo, Kinetic study of the hydrogen oxidation reaction on Pt over the complete overpotential range, Journal of Power Sources 229 (2013) 210–215.
[25] H. Kita, Y. Gao, T. Nakato, H. Hattori, Effect of hydrogen sulphate ion on the hydrogen ionization and methanol oxidation reactions on platinum single-crystal electrodes, Journal of Electroanalytical Chemistry 373 (1994) 177–183.
[26] J. Omura, H. Yano, M. Watanabe, H. Uchida, Electrochemical Quartz Crystal Microbalance Analysis of the Oxygen Reduction Reaction on Pt-Based Electrodes. Part 1: Effect of Adsorbed Anions on the Oxygen Reduction Activities of Pt in HF, HClO4, and H2SO4 Solutions, Langmuir 27 (2011) 6464–6470.
[27] G.K.H. Wiberg, M. Arenz, Establishing the potential dependent equilibrium oxide coverage on platinum in alkaline solution and its influence on the oxygen reduction, Journal of Power Sources 217 (2012) 262–267.
[28] E.W. Washburn, Electrical Conductivity of Aqueous Solutions, International Critical Tables of Numerical Data, Physics, Chemistry and Technology (1st Electronic Edition), Knovel, 1926–1930.
[29] K. Aoki, A. Baars, A. Jaworski, J. Osteryoung, Chronoamperometry of strong acids without supporting electrolyte, Journal of Electroanalytical Chemistry 472 (1999) 1–6.

[30] K. Aoki, A. Tokida, Resistance of solution without supporting electrolyte under the reduction of HCl, Electrochimica Acta 45 (2000) 3483–3488.
[31] J. Durst, A. Siebel, C. Simon, F. Hasche, J. Herranz, H.A. Gasteiger, New insights into the electrochemical hydrogen oxidation and evolution reaction mechanism, Energy & Environmental Science 7 (2014) 2255–2260.
[32] W. Sheng, Z. Zhuang, M. Gao, J. Zheng, J.G. Chen, Y. Yan, Correlating hydrogen oxidation and evolution activity on platinum at different pH with measured hydrogen binding energy, Nat Commun 6 (2015) .
[33] J.K. Nørskov, T. Bligaard, A. Logadottir, S. Bahn, L.B. Hansen, M. Bollinger, H. Bengaard, B. Hammer, Z. Sljivancanin, M. Mavrikakis, Y. Xu, S. Dahl, C.J.H. Jacobsen, Universality in Heterogeneous Catalysis, Journal of Catalysis 209 (2002) 275–278.
[34] E. Gileadi, S.D. Argade, J.O.M. Bockris, The Potential of Zero Charge of Platinum and Its pH Dependence, The Journal of Physical Chemistry 70 (1966) 2044–2046.
[35] M.R. Gennero de Chialvo, A.C. Chialvo, Hydrogen diffusion effects on the kinetics of the hydrogen electrode reaction. Part I. Theoretical aspects, Physical Chemistry Chemical Physics 6 (2004) 4009–4017.
[36] P.M. Quaino, J.L. Fernández, M.R. Gennero de Chialvo, A.C. Chialvo, Hydrogen oxidation reaction on microelectrodes: Analysis of the contribution of the kinetic routes, Journal of Molecular Catalysis A: Chemical 252 (2006) 156–162.
[37] J.X. Wang, T.E. Springer, R.R. Adzic, Dual-Pathway Kinetic Equation for the Hydrogen Oxidation Reaction on Pt Electrodes, Journal of The Electrochemical Society 153 (2006) A1732–A1740.
[38] A.N. Frumkin, O.A. Petrii, Potentials of zero total and zero free charge of platinum group metals, Electrochimica Acta 20 (1975) 347–359.
[39] V.c. Climent, R. Gómez, J.M. Feliu, Effect of increasing amount of steps on the potential of zero total charge of Pt(111) electrodes, Electrochimica Acta 45 (1999) 629–637.
[40] V. Climent, G.A. Attard, J.M. Feliu, Potential of zero charge of platinum stepped surfaces: a combined approach of CO charge displacement and N2O reduction, Journal of Electroanalytical Chemistry 532 (2002) 67–74.
[41] H.A. Gasteiger, N.M. Markovic, P.N. Ross, H2 and CO Electrooxidation on Well-Characterized Pt, Ru, and Pt-Ru. 1. Rotating Disk Electrode Studies of the Pure Gases Including Temperature Effects, The Journal of Physical Chemistry 99 (1995) 8290–8301.
[42] G.J. Janz, B.G. Oliver, G.R. Lakshminarayanan, G.E. Mayer, Electrical conductance, diffusion, viscosity, and density of sodium nitrate, sodium perchlorate, and sodium thiocyanate in concentrated aqueous solutions, The Journal of Physical Chemistry 74 (1970) 1285–1289.
[43] H.A. Gasteiger, J.E. Panels, S.G. Yan, Dependence of PEM fuel cell performance on catalyst loading, Journal of Power Sources 127 (2004) 162–171.